



Geophysical Research Letters

RESEARCH LETTER

10.1002/2017GL076916

Key Points:

- Internal tidal dynamics are investigated with a high-resolution numerical model
- Tidally induced internal waves explain 92% of the total internal wave flux over the Izu-Ogasawara Ridge, off the Japan mainland
- Approximately 30% of the total kinetic energy is excited by tidal forcing over the ridge

Supporting Information:

- Supporting Information S1

Correspondence to:

E. Masunaga,
ejji.masunaga.office@vc.ibaraki.ac.jp

Citation:

Masunaga, E., Uchiyama, Y., Suzue, Y., & Yamazaki, H. (2018). Dynamics of internal tides over a shallow ridge investigated with a high-resolution downscaling regional ocean model. *Geophysical Research Letters*, 45, 3550–3558. <https://doi.org/10.1002/2017GL076916>

Received 21 DEC 2017

Accepted 27 MAR 2018

Accepted article online 31 MAR 2018

Published online 16 APR 2018

Dynamics of Internal Tides Over a Shallow Ridge Investigated With a High-Resolution Downscaling Regional Ocean Model

Eiji Masunaga¹ , Yusuke Uchiyama² , Yota Suzue³, and Hidekatsu Yamazaki⁴ 

¹Center for Water Environment Studies, Ibaraki University, Hitachi, Japan, ²Department of Civil Engineering, Kobe University, Kobe, Japan, ³CTI Engineering Co., Ltd., Nagoya, Japan, ⁴Department of Ocean Science, Tokyo University of Marine Sciences and Technology, Tokyo, Japan

Abstract This study investigates the dynamics of tidally induced internal waves over a shallow ridge, the Izu-Ogasawara Ridge off the Japanese mainland, using a downscaled high-resolution regional ocean numerical model. Both the Kuroshio and tides contribute to the field of currents in the study area. The model results show strong internal tidal energy fluxes over the ridge, exceeding 3.5 kW m^{-1} , which are higher than the fluxes along the Japanese mainland. The flux in the upstream side of the Kuroshio is enhanced by an interaction of internal waves and currents. The tidal forcing induces 92% of the total internal wave energy flux, exhibiting the considerable dominance of tides in internal waves. The tidal forcing enhances the kinetic energy, particularly in the northern area of the ridge where the Kuroshio Current is not a direct influence. The tidal forcing contributes to roughly 30% of the total kinetic energy in the study area.

Plain Language Summary Internal waves are ubiquitous phenomena in oceans, and they play a significant role in global ocean circulations and climates. However, details of internal waves have not been understood well due to limitations of field surveys. This study investigates the dynamics of tidally induced internal waves (internal tides) over a shallow ridge using a high-resolution numerical simulator with a horizontal resolution of 1 km. The model results show that tidal forcing dominates in internal wave energy over the ridge, and an interaction of internal waves and currents enhances internal waves in the upstream side of the Kuroshio. Internal tides explain 92% of the total internal wave flux over the ridge. Tides generate roughly 30% of the total kinetic energy in the study area.

1. Introduction

Tidally induced internal waves, namely, internal tides, are important phenomena in oceanic physical processes. Internal tides enhance their nonlinearity as they propagate into shallow regions, resulting in pronounced mass transports (e.g., Masunaga, Arthur, et al., 2017) and turbulent mixing (e.g., MacKinnon & Gregg, 2003). Recent studies have revealed the dynamics and mechanisms of nonlinear internal tides in shallow regions, using both observational and numerical approaches. The observational studies have found several processes associated with nonlinear or breaking internal tides in shallow slopes, resulting in strong sediment resuspension and turbulent mixing due to strongly enhanced shear flows (e.g., Cheriton et al., 2014; Masunaga et al., 2016). Although signals of nonlinear internal tides have occasionally been observed by mooring systems, it is generally difficult to understand all the processes involved with internal tides, including their generation, propagation, and dissipation, from spatially sparse observations. By contrast, numerical simulations are better suited to investigate these processes. Recent modeling studies have succeeded in examining shelf-scale generation, propagation, and dissipation processes of internal tides (e.g., Kang & Fringer, 2012; Masunaga, Fringer, et al., 2017; Varlamov et al., 2015).

In this study, we conducted numerical simulations to investigate internal tidal dynamics over the Izu-Ogasawara Ridge that extends southward from the Japanese mainland (Figure 1a). This shallow ridge is largely influenced by both the western boundary current (Kuroshio) and tides. The Kuroshio Current passes over the ridge from west to east at a maximum speed of about 2 m s^{-1} (e.g., Uchiyama, Kanki, et al., 2017). Barotropic (BT) tidal waves are known to propagate from east to west over the ridge, which results in strong tidal flows. In addition, this area is known as an important area for maintaining marine ecosystems in the Northwest Pacific Ocean, because of strong mass transport and mixing over the shallow ridge (e.g., Hasegawa et al., 2004). Masunaga, Fringer, et al. (2017) reported that tidal flows induce highly nonlinear internal tides in this area. It has also been reported that the intensity of internal tides over the ridge is much higher

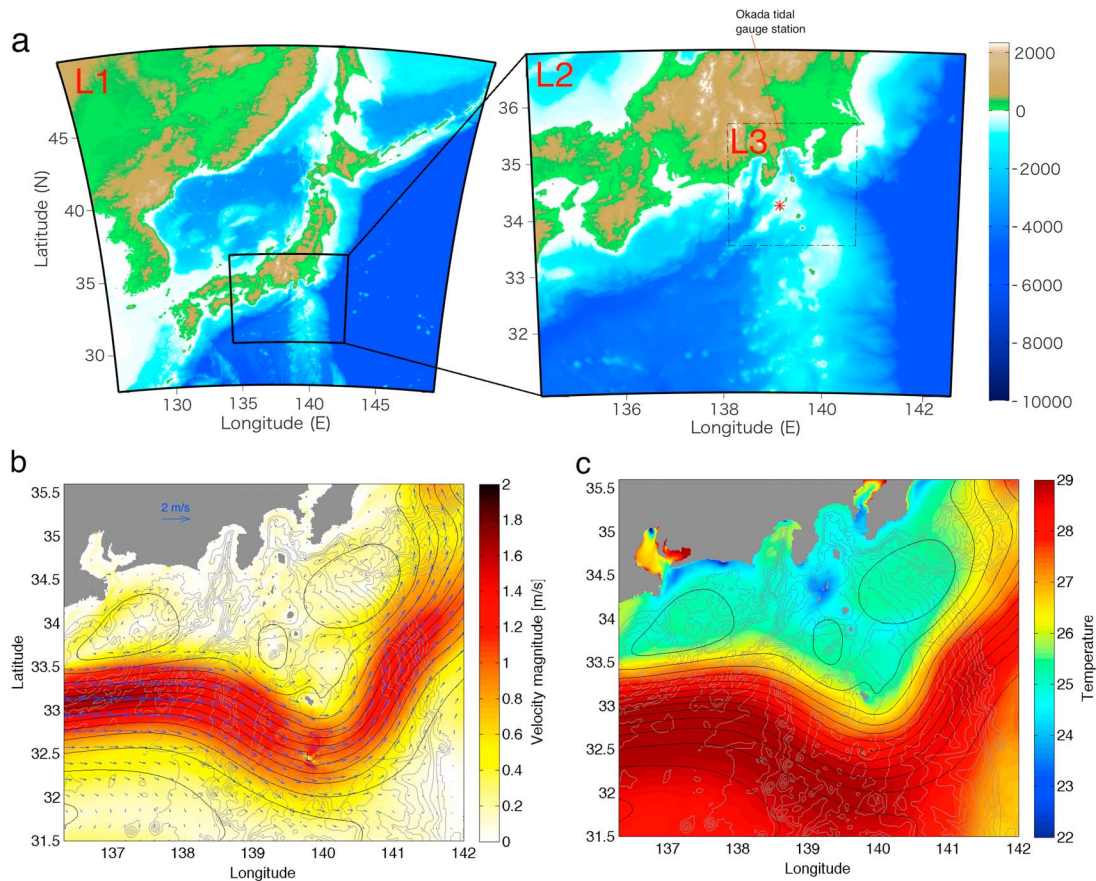


Figure 1. (a) Numerical domains and topography for the (left) ROMS-L1 and (right) ROMS-L2 models. The temporally averaged L2 results for 21 July 21 to 4 August 2013 from Run #1 for (b) the subsampled surface velocity vectors with their magnitudes in color and (c) sea-surface temperatures (color). The solid black and thin gray contours in (b) and (c) show the time-averaged sea surface height at intervals of 0.1 m with isobaths spaced at intervals of 500 m. The black dotted box shown in (a) indicates the L3 domain used for the sensitive test described in the supporting information.

than it is along the Japanese mainland (Masunaga, Fringer, et al., 2017; Varlamov et al., 2015). Varlamov et al. (2015) conducted numerical modeling of M_2 internal tides with a horizontal resolution of $1/36^\circ$ (~ 3 km), which may not be sufficiently fine to reveal details of the internal tide dynamics, particularly in coastal areas. Thus, Masunaga, Fringer, et al. (2017) instead used a high-resolution, triangle unstructured grid numerical model (SUNTANS) with greatly idealized forcings. High-resolution models with realistic oceanic conditions are necessary for understanding the details and effects of internal tides over the ridge. This study investigates the internal tidal dynamics over the Izu-Ogasawara Ridge, using a high-resolution downscaled Regional Oceanic Modeling System (ROMS) with a staggered horizontal grid coordinate under realistic oceanic and atmospheric forcings.

2. Model Configurations

Numerical simulations were performed with a double-nested configuration, based on a research version of ROMS (e.g., Shchepetkin & McWilliams, 2005). The outer domain (ROMS-L1) is embedded in the daily-averaged Japan Coastal Ocean Predictability Experiment 2 (JCOPE2) oceanic reanalysis product (Miyazawa et al., 2009). The horizontal grid spacing of 3 km and the vertically stretched 32 layers in the s -coordinate are used for the L1 model. The L1 model is forced by realistic surface wind stresses, surface fluxes, and river discharges (see Uchiyama, Suzue, & Yamazaki, 2017, for more details). The high-resolution L2 model with a horizontal grid spacing of 1 km is nested in the L1 model using a one-way offline nesting technique (e.g., Mason et al., 2010). The L2 model consists of 800×674 horizontal cells with 40 vertical s -coordinate layers. The open boundaries of the L2 model are forced by sea surface height and three-dimensional horizontal

currents and scalars (temperature and salinity) from the parent L1 model output. In addition, BT tidal forcing estimated from the TPXO 7.0 tide model (Egbert & Erofeeva, 2002) is imposed along the perimeter of the L2 model. Baroclinic (BC) tides inclusive of internal tides are thus spontaneously computed in the L2 model with realistic large-scale influences, such as those from the Kuroshio Current. The amplitudes and phases of the tidal forcing were corrected using Newton's method to improve the reproducibility of tidal signals (see details in the Appendix of Masunaga, Fringer, et al., 2017). The ocean surface is forced by hourly wind stress (from the Japan Meteorological Agency Grid Point Value Mesoscale Model) and monthly climatological surface heat, freshwater fluxes, and radiation fluxes (from the National Oceanic and Atmospheric Administration Comprehensive Ocean-Atmosphere Data Set, NOAA-COADS; Woodruff et al., 1987). Monthly averaged climatological freshwater discharges are added as point sources of freshwater and mass from 31 river mouths located along the coast in the L2 domain. The K-Profile Parameterization mixed-layer turbulence model is employed for computing vertical momentum eddy viscosity and scalar eddy diffusivity (Large et al., 1994). Horizontal eddy momentum viscosity and scalar eddy diffusivity are set at $0 \text{ m}^2 \text{ s}^{-1}$, except for in the small background hyper viscosity and diffusivity associated with an upstream-biased third-order advection scheme in ROMS. To maintain numerical stability, the BC time step size is set to 30 s for the L2 model.

To investigate the effects of the tides, Kuroshio Current, and winds separately, three model runs were conducted in this study: Run #1 is the baseline case in which all the forcing (three-dimensional flows and tides along the open boundaries, winds, and heat and freshwater fluxes at surface) is considered in the model to be as realistic as possible, Run #2 is the same as Run #1 but without tides, and Run #3 is the same as Run #1 but without tides and winds. The L2 model was spun-up from 29 December 2011 to 30 July 2013 without tides. Then, the tidal forcing was imposed starting on 1 July 2013, and the tidal computation was carried out for 2 months. The model output from 21 July until 10 August is used in the following analyses, and thus, the first 3 weeks are excluded as the model spin-up with tides takes place. A sensitivity test of the horizontal grid resolution (grid spacing of 1 km and 300 m) was also conducted to investigate effects of the model resolution on numerical results. The sensitivity test showed that differences of the kinetic energy (KE) and internal wave flux in these two model cases are only a few percent (see supporting information).

The oceanic model used in this study, ROMS, has extensively been validated for the Kuroshio regions in previous studies (e.g., Kamidaira et al., 2017; Uchiyama, Kanki, et al., 2017; Uchiyama, Suzue, & Yamazaki, 2017) to demonstrate that the model can reproduce the Kuroshio Current and mesoscale and submesoscale eddies with high accuracy. The computed tidal elevations in the L2 model are compared with the observed data at the Okada tidal gauge station located on Izu-Oshima Island (Figure 1a). The root-mean-square error (E) between the modeled and observed tides can be estimated by the following formula (Carter, 2010):

$$E = \sqrt{\frac{1}{2}(a_O^2 + a_M^2) - a_O a_M \cos(G_O - G_M)} \quad (1)$$

where a is the tidal amplitude, G is the phase, and the subscripts O and M denote observations and predictions by the model, respectively. The estimated E for the four major tidal constituents— S_2 , M_2 , K_1 , and O_1 —is 0.013, 0.004, 0.020, and 0.016 m, respectively. The relative error, E/a_O , is 7.8%, 1.2%, 9.0%, and 10.0% for S_2 , M_2 , K_1 , and O_1 , respectively (the mean error of 7.0%). BT surface tidal motions can be validated by using observed data obtained from tidal gauge stations or global tidal models; however, it is difficult to obtain large-scale BC internal tidal motions due to the limitation of field surveys. Furthermore, the area around the Izu-Ogasawara ridge is known as a great fishing ground; mooring surveys in this area are limited by fishery communities. Although the modeled data are not validated with BC internal motions, we assume that the model performance is sufficient for investigating internal tidal dynamics in the study area.

3. Internal Waves Over the Ridge

The model results show that the interaction of BT tides and the shallow ridge generates strong tidal flows, leading to internal tidal generations. Figures 2a–2d show time series of sea surface height, temperature, and BC flow components at the point shown by the red asterisk in Figure 1a. Large isothermal displacements, accompanied by strong BC flows, reaching 0.8 m s^{-1} , appear during the spring tides around 24 July and 7 August. The isothermal displacements exceed 50 m where the depth is $\sim 120 \text{ m}$, which is approximately

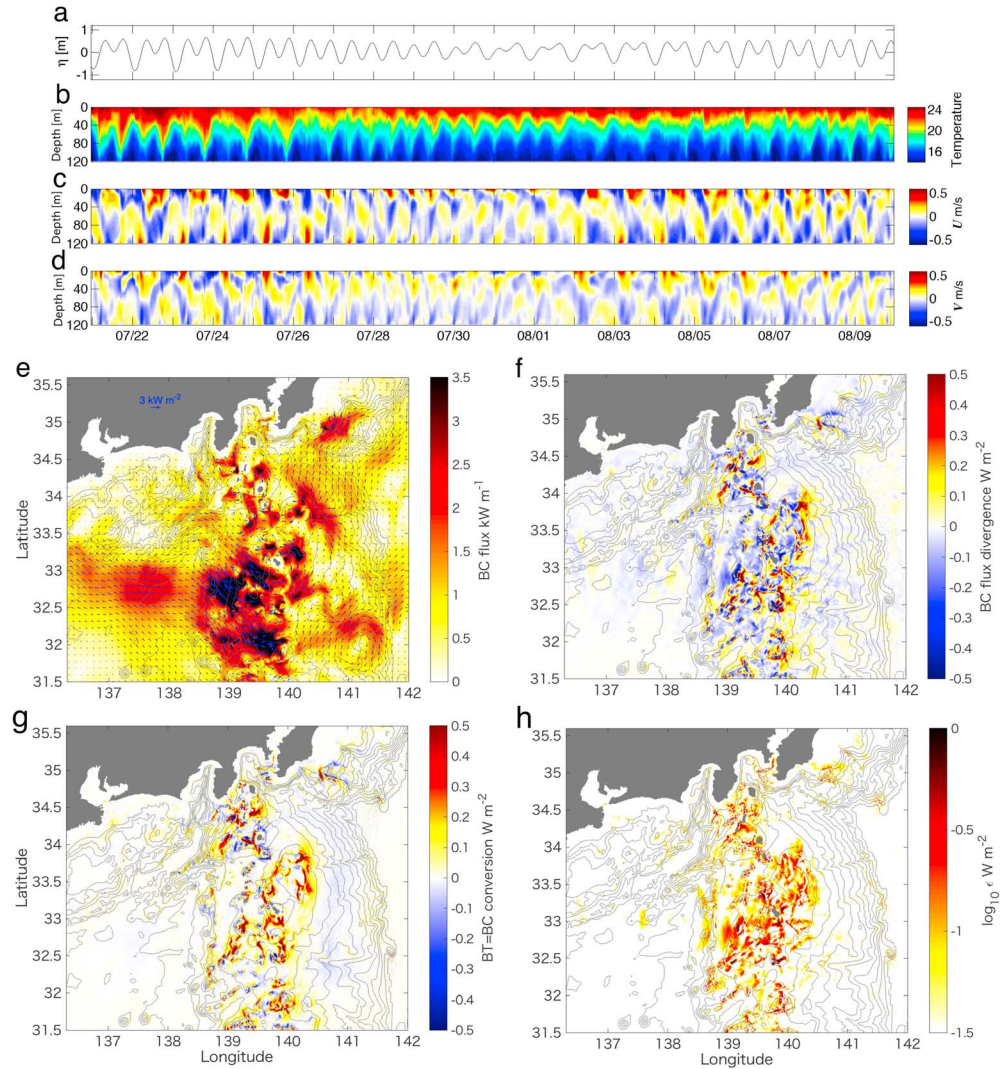


Figure 2. Results from Run #1. (a) Tidal elevation, (b) temperature, and the (c) eastward (zonal) and (d) northward (meridional) components of baroclinic velocity at the location indicated by the red asterisk shown in Figure 1a (right). (e) Time-averaged and vertically integrated internal wave flux, (f) the divergence of internal wave flux, (g) the barotropic to baroclinic conversion rate, and (h) the baroclinic dissipation rate. The gray contours in (e)–(h) are isobaths spaced at intervals of 500 m.

25 times larger than surface elevations. To investigate the energetics of internal waves, the BC internal wave energy flux is computed. The dominant BC flux is expressed as follows (Kang & Fringer, 2012):

$$F_E = p' \mathbf{u}'_{BC}, \quad (2)$$

where p is the pressure, \mathbf{u}_{BC} is the BC velocity, and the prime denotes the perturbation component within the internal wave frequency. The perturbation p' and \mathbf{u}'_{BC} are defined for frequencies higher than $3.86 \times 10^{-6} \text{ s}^{-1}$ (i.e., a period of less than 72 hr) to include tidal signals and their harmonics. Figure 2e shows the time-averaged and depth-integrated BC flux, $\langle \overline{F_E} \rangle$, where the over bar denotes a depth-integral operator, and the brackets indicate a time-averaging operator; Figure 2f shows the divergence of the BC flux, $\nabla_H \cdot \langle \overline{F_E} \rangle$, over 2 weeks (~one spring-neap cycle, 21 July 21 to 4 August). Strongly enhanced internal wave fluxes are distributed along the ridge. The intensity of the flux exceeds 3.5 kW m^{-1} , which is consistent with the results found in Masunaga, Fringer, et al. (2017).

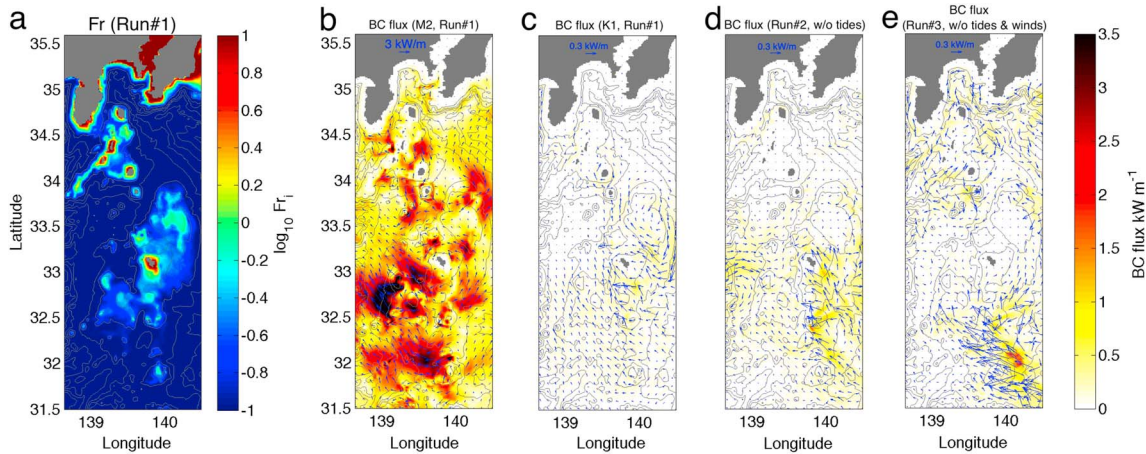


Figure 3. (a) The maximum internal Froude number from Run #1, the (b) semidiurnal and (c) diurnal internal wave flux from Run #1, (d) the internal wave flux from Run #2 (w/o tides), and (e) the internal wave flux from Run #3 (w/o tides and winds). The gray contours are isobaths spaced at intervals of 500 m.

The high westward BC flux appears in the upstream (i.e., western) side of the Kuroshio Current, with its direction opposing that of the Kuroshio Current (Figure 2e, $\sim 137.5^\circ\text{E}$, 33°N). For surface gravity waves, it is well known that the wave amplitude increases when the wave direction is opposite to the direction of background currents (e.g., Mei, 1992). Recent idealized numerical experiments by Lamb and Dunphy (2018) showed that an interaction of internal waves and background currents enhances the upstream internal wave flux from a ridge. The high BC flux in the upstream side of the Kuroshio Current is supposed to be generated by an interaction of internal tides and the Kuroshio.

The time-averaged and depth-integrated BT to BC (BT-BC) conversion rate (\overline{C}) and BC dissipation rate ($\overline{\varepsilon}$) are given by (Kang & Fringer, 2012)

$$\langle \overline{C} \rangle = \langle \overline{\rho' g W'} \rangle, \quad (3)$$

$$\langle \overline{\varepsilon} \rangle = \nabla_H \cdot \langle \overline{F_E} \rangle - \langle \overline{C} \rangle, \quad (4)$$

where ρ' is the perturbation density and W is the BT vertical velocity ($W = -\nabla_H \cdot [(d+z)\mathbf{U}_H]$, where d is the total depth and \mathbf{U}_H is the depth-averaged lateral BT velocity). The magnitude of both the BT-BC conversion rate ($\langle \overline{C} \rangle$) and dissipation rate ($\langle \overline{\varepsilon} \rangle$) is high over the ridge. They show a patchy structure where amplified $\langle \overline{C} \rangle$ and $\langle \overline{\varepsilon} \rangle$ manifest next to each other, corresponding to negative and positive values of the divergence of the internal tides. This implies that the internal waves mostly dissipate where they are generated. Therefore, the generated internal waves contribute to mixing processes near their local generation sites. On the other hand, although the intensity is not high, the internal wave energy radiates away from the ridge, for example, as the westward flux on the upstream side of the Kuroshio Current. Such offshore-ward internal wave propagations are believed to contribute to deep ocean mixing processes.

The shape of the isotherm displacements is vertically asymmetric, which suggests the appearance of nonlinear internal waves that include high-frequency components (Figure 2b, especially during the spring tides, around 24 July and 7 August). Such nonlinear internal waves occur when they propagate along shallow regions, and the internal Froude number ($Fr_i = U_H/c_i$, where U_H is the horizontal BT flow speed and c_i is the internal wave speed) exceeds the critical value of 1 (e.g., Hibiya, 1986; Masunaga, Fringer, et al., 2017; Venayagamoorthy & Fringer, 2006). The maximum Fr_i is plotted in Figure 3a, showing the critical value over the ridge where the total depth d is less than 500 m. Strong internal waves under the high Froude number condition are anticipated to lead to highly nonlinear wave motions over the ridge, such as those shown in Figure 2b.

In order to investigate the frequency responses of internal waves, the BC flux was computed from band-pass-filtered data for the frequencies of semidiurnal ($\sim M_2$ and S_2) and diurnal ($\sim K_1$ and O_1) bands (Figures 3b and 3c). The semidiurnal BC flux shows strong internal waves over the ridge, and its spatial structure explains that

of the total internal wave flux shown in Figure 2e. The magnitude of the semidiurnal (diurnal) BC flux contributes to ~73% (~5%) of the total internal wave flux integrated over the ridge. Because the study area is located in midlatitudes, the diurnal waves can propagate only as Kelvin waves trapped along shallow topography. Masunaga, Fringer, et al. (2017) reported that the resonance of the internal Kelvin waves (i.e., diurnal internal tides) occurs around an island located on the Izu-Ogasawara Ridge if the wavelength matches the island's scale, which results in a largely enhanced, diurnal, internal tidal energy. However, the intensity of the diurnal internal tides is much lower than that of the semidiurnal internal tides in this result. The stratification (i.e., buoyancy frequency) in our simulation period may not satisfy the resonance condition of island-trapped internal tides.

Internal waves are generated not only by tides but also by strong geostrophic flows (inertial currents, e.g., the Kuroshio Current) and winds. Recent studies have suggested that near-inertial internal waves play important roles in the vicinity of the Kuroshio Current (e.g., Nagai et al., 2015). In addition, winds are known to be sources of internal waves (e.g., Kitade & Matsuyama, 2000). In order to evaluate the effects of tides, the Kuroshio Current, and winds on internal wave dynamics, we compare the BC fluxes from the three model runs (Figures 2e and 3d and 3e). The BC fluxes for Runs #2 and #3 are much lower than the flux in the run with tidal forcing (Run #1). For the case without tidal forcing (Run #2), although the internal wave energy flux reaches $\sim 1.5 \text{ kW m}^{-1}$ in the Kuroshio Current path around the latitudes of $32\text{--}33.5^\circ\text{N}$, the flux over the ridge is much lower than it is for the case with tidal forcing (Run #1). The spatially averaged internal wave flux over the ridge for Run #2 (without tidal forcing) is 8% of that for Run #1, in which ~92% of the internal wave flux is induced by the tidal forcing. Therefore, the intensity of the internal tides is much higher than the intensity of the internal waves due to the Kuroshio Current and winds (near the inertial internal waves and wind-induced internal waves). The 92% of the total internal wave flux caused by tides is 14% higher than the sum of semidiurnal ($\sim M_2$) and diurnal ($\sim K_1$) internal wave fluxes (78%). This difference implies that nonlinear or higher harmonic internal tides contribute to 14% of the total internal wave flux.

The spatially averaged internal wave flux for the case without tides and wind (Run #3) is slightly higher (6%) than for the case without tides (Run #2). This suggests that winds do not enhance the internal waves, but rather act to dissipate their energy. The vertical eddy viscosity and diffusivity estimated by the K-Profile Parameterization model are considerably reduced by design if wind stress is omitted, because eddy viscosity and diffusivity are computed based on wind stress and buoyancy flux at the ocean surface (e.g., Large et al., 1994). This condition results in small vertical eddy viscosity and diffusivity that cause less damping of the internal waves for Run#3.

4. Kinetic Energy

The time-averaged KE density ($\langle \overline{\rho \mathbf{u}^2} / (2d) \rangle$, where ρ is the water density) is plotted in Figure 4 (Figures 4a and 4b show the results from Runs #1 and #2, respectively). The Kuroshio Current causes high KE density along its path. The highest KE density of $\sim 10^3 \text{ J m}^{-3}$ appears where the Kuroshio Current passes over the shallow ridge at approximately 33°N and 140°E , with a maximum flow speed of approximately 2 m s^{-1} . The KE density is also high around the islands located on the northern ridge at around $34\text{--}35^\circ\text{N}$ and near the mouths of the Tokyo Bay and Ise Bay for the tidal forcing case (Run #1). On the other hand, the KE density in these areas is lower in the case without tidal forcing than it is for the tidal forcing case. The differences in the KE are represented in Figure 4c as the ratios of the KE density between the case with the tidal forcing (Run #1, KE_{Tide}) and the case without the tidal forcing (Run #2, $\text{KE}_{\text{w/o Tide}}$). Figure 4c demonstrates that the tidal forcing enhances the KE by a factor of 10 over the northern ridge. Thus, tidal forcing dominates the KE over the northern ridge where the Kuroshio Current does not have direct influences. Nevertheless, the difference between the KE of Runs #1 and #2 is rather small along the Kuroshio Current path, suggesting that the Kuroshio Current has a more dominant effect on the increased KE in this area than do the tides.

The KE is divided into the BT and BC components as follows:

$$\text{KE}_{\text{Total}} = \text{KE}_{\text{BT}} + \text{KE}_{\text{BC}} + \text{KE}_{\text{BTBC}} \quad (5)$$

$$\text{KE}_{\text{BT}} = \frac{1}{2} \rho (U^2 + V^2) \quad (6)$$

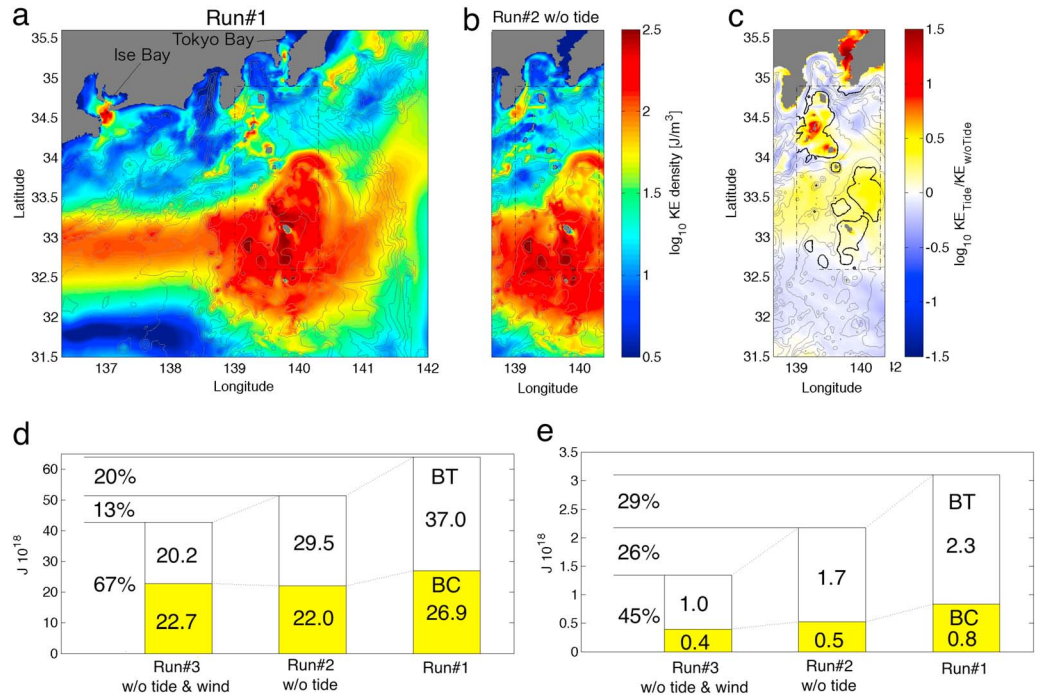


Figure 4. The kinetic energy (KE) density for (a) Run #1 and (b) Run #2 (w/o tides), (c) the ratio of the depth-integrated KE between Runs #1 and #2, and (d) the volume-integrated KE_{BT} (white bars) and KE_{BC} (yellow bars) over the ridge area denoted by the black dotted box. (e) Same as (d), but in the area shallower than 500 m depicted by the thick gray contours in (c). The numbers labeled on the bars in (d) and (e) are the integrated KE_{BT} and KE_{BC} for each case (units of $\times 10^{18}$ J). Note that KE_{BT} and KE_{BC} are defined by equations (6) and (7).

$$\text{KE}_{\text{BC}} = \frac{1}{2} \rho (u'^2 + v'^2 + w'^2) \quad (7)$$

$$\text{KE}_{\text{BTBC}} = \rho (Uu' + Vv') \quad (8)$$

where U and V are depth-averaged BT lateral velocities, u' and v' are horizontal BC velocities, and KE_{BTBC} represents the cross term eliminated by the depth integration (Kang & Fringer, 2012).

Figure 4d shows the time-averaged and volume-integrated KE_{BT} and KE_{BC} over the ridge, represented by the black dotted box in Figures 4a–4c for the three cases. Figure 4e is the same as Figure 4d, but only for areas shallower than 500 m, depicted by the thick gray contours in Figure 4c. The more types of forcing the model includes, the more total KE increases. In Figure 4d, KE_{Total} for Run #3 is about 67% of that for Run #1, suggesting that 2/3 of KE_{Total} in the entire ridge area is generated neither by tides nor by wind, but by the Kuroshio Current. KE_{BC} for Run #3 explains 36% of the KE_{Total} , presumably due to the baroclinicity associated with the vertical shear of the Kuroshio Current (e.g., Uchiyama, Kanki, et al., 2017) rather than the internal waves, as shown in Figure 3e. From the difference between Runs #3 and #2, the wind forcing is found to explain approximately 13% of the KE_{Total} for Run #1, which mainly contributes to KE_{BT} . Similarly, the tidal forcing significantly enhances both KE_{BT} and KE_{BC} , which respectively explain 12% and 8% of the KE_{Total} for Run #1. The increase in KE_{BC} by the tidal forcing can apparently be attributed to energetic internal tides.

In the shallow areas (Figure 4e), the relative contributions from the winds and tides to KE_{Total} are greater than those in the whole ridge area shown in Figure 4d. Winds and tides (BT + BC) explain 26% and 29% of KE_{Total} for Run #1, respectively, whereas the contributions of BT and BC (internal) tides are 19% and 10%, respectively. These results demonstrate that both the local wind stress and BT tides, which are amplified around the ridge topography, more significantly contribute to the KE_{Total} in the shallow area. The contribution of the internal tides is significant by similar amplitude in both depth ranges. The contribution is 10% for the shallow area, as shown in Figure 4e, whereas it is not considerably reduced in the deep ocean (at 8%) for the entire ridge area in Figure 4d.

5. Summary

High-resolution numerical experiments were conducted with a double-nested JCOPE2-ROMS downscaling system to investigate the internal wave dynamics over a shallow ridge influenced by tides and the Kuroshio Current. We chose to investigate the Izu-Ogasawara Ridge that extends southward from the Japanese main island and crosses the Kuroshio Current path. The model realistically showed details of the internal wave structure over the ridge and revealed that 78% of the total internal wave (BC) flux over the ridge is dominated by semidiurnal ($\sim S_2$ and M_2) internal tides. Meanwhile, the contributions from diurnal ($\sim K_1$ and O_1) tides, winds, and geostrophic flows (e.g., the Kuroshio Current) to the internal waves are much less than those from the semidiurnal internal tides. Internal tides explain 92% of the total internal wave fluxes. The internal Froude number exceeds the critical value, which results in highly nonlinear internal wave motions on the shallow ridge. The internal tidal flux in the upstream side of the Kuroshio is enhanced by an interaction of internal tides and currents. Approximately 30% and 10% of the total KE are generated by the tides (BT + BC) and internal tides (BC), respectively. Especially over the shallow northern ridge, the tidal forcing enhances the KE by a factor of 10.

The tidal forcing is sometimes neglected in developing global/regional oceanic models to simplify model configurations; however, this study indicates that tidal forcing contributes to roughly 30% of the total KE over a shallow ridge. In addition, internal tides dominate approximately half of the tidally induced KE, and they also contribute to deep ocean mixing processes. This study suggests that tides and internal tides play significant roles in oceanic physical processes, and they must be considered to better understand, for example, energy budgets and mixing processes in the ocean.

Acknowledgments

This study was supported by JST-CREST grant JPRMJCR12A6. E. Masunaga acknowledges the JSPS Grant-in-Aid for Scientific Research (15K06227). Y. Uchiyama also acknowledges JSPS Grant-in-Aid for Scientific Research (15K0207 and 15H04049). The ROMS model used in this study is distributed by its developers and is available at <https://www.myroms.org/>. The JCOPE2 reanalysis data are available for scientific research purposes from Japan Agency for Marine-Earth Science and Technology (JAMSTEC) and are available at <http://www.jamstec.go.jp/jcope2/htdocs/e/distribution/index.html>. The JMA GPV-MSM data set is provided by Japan Meteorological Agency (JMA) and is available at <http://database.rish.kyoto-u.ac.jp/arch/jmadata/data/gpv/original/>. The NOAA-COADS climatological data set is distributed by NOAA at <https://www.esrl.noaa.gov/psd/data/gridded/data.coads.1deg.html>. TPXO tidal data set is available at <http://volkov.oce.orst.edu/tides/>.

References

- Carter, G. S. (2010). Barotropic and baroclinic M2 tides in the Monterey Bay region. *Journal of Physical Oceanography*, 40(8), 1766–1783. <https://doi.org/10.1175/2010JPO4274.1>
- Cheriton, O. M., McPhee-Shaw, E. E., Shaw, W. J., Stanton, T. P., Bellingham, J. G., & Storlazzi, C. D. (2014). Suspended particulate layers and internal waves over the southern Monterey Bay continental shelf: An important control on shelfmud belts. *Journal of Geophysical Research: Oceans*, 119, 428–444. <https://doi.org/10.1002/2013JC009360>
- Egbert, G. D., & Erofeeva, S. Y. (2002). Efficient inverse modeling of barotropic ocean tides. *Journal of Atmosphere and Oceanic Technology*, 19(2), 183–204. [https://doi.org/10.1175/1520-0426\(2002\)019%3C0183:EIMOB0%3E2.0.CO;2](https://doi.org/10.1175/1520-0426(2002)019%3C0183:EIMOB0%3E2.0.CO;2)
- Hasegawa, D., Yamazaki, H., Lueck, R. G., & Seuront, L. (2004). How islands stir and fertilize the upper ocean. *Geophysical Research Letters*, 31, L16303. <https://doi.org/10.1029/2004GL020143>
- Hibiya, T. (1986). Generation mechanism of internal waves by tidal flow over a sill. *Journal of Geophysical Research*, 91(C6), 7697–7708. <https://doi.org/10.1029/JC091iC06p07697>
- Kamidaira, Y., Uchiyama, Y., & Mitarai, S. (2017). Eddy-induced transport of the Kuroshio warm water around the Ryukyu Islands in the East China Sea. *Continental Shelf Research*, 143, 206–218. <https://doi.org/10.1016/j.csr.2016.07.004>
- Kang, D., & Fringer, O. (2012). Energetics of barotropic and baroclinic tides in the Monterey Bay area. *Journal of Physical Oceanography*, 42(2), 272–290. <https://doi.org/10.1175/JPO-D-11-039.1>
- Kitade, Y., & Matsuyama, M. (2000). Coastal-trapped waves with several-day period caused by wind along the southeast coast of Honshu, Japan. *Journal of Oceanography*, 56, 727–744.
- Lamb, K. G., & Dunphy, M. (2018). Internal wave generation by tidal flow over a two-dimensional ridge: Energy flux asymmetries induced by a steady surface trapped currents. *Journal of Fluid Mechanics*, 836, 192–221. <https://doi.org/10.1017/jfm.2017.800>
- Large, W. G., McWilliams, J. C., & Doney, S. C. (1994). Oceanic vertical mixing: A review and a model with a nonlocal boundary layer parameterization. *Reviews of Geophysics*, 32(4), 363–403. <https://doi.org/10.1029/94RG01872>
- MacKinnon, J. A., & Gregg, M. C. (2003). Mixing on the late-summer New England shelf—Solibores, shear, and stratification. *Journal of Physical Oceanography*, 33(7), 1476–1492.
- Mason, E., Molemaker, J., Shchepetkin, A. F., Colas, F., McWilliams, J. C., & Sangrà, P. (2010). Procedures for offline grid nesting in regional ocean models. *Ocean Modelling*, 35(1-2), 1–15. <https://doi.org/10.1016/j.ocemod.2010.05.007>
- Masunaga, E., Arthur, R. S., Fringer, O. B., & Yamazaki, H. (2017). Sediment resuspension and generation of intermediate nephew layers by shoaling internal bores. *Journal of Marine Systems*, 170, 31–41. <https://doi.org/10.1016/j.jmarsys.2017.01.017>
- Masunaga, E., Fringer, O. B., Kitade, Y., Yamzaki, H., & Gallager, S. M. (2017). Dynamics and energetics of trapped diurnal internal Kelvin waves around a mid-latitude island. *Journal of Physical Oceanography*, 47(10), 2479–2498. <https://doi.org/10.1175/JPO-D-16-0167.1>
- Masunaga, E., Fringer, O. B., Yamazaki, H., & Amakasu, K. (2016). Strong turbulent mixing induced by internal bores interacting with internal tide-driven vertically-sheared flow. *Geophysical Research Letters*, 43, 2094–2101. <https://doi.org/10.1002/2016GL067812>
- Mei, C. C. (1992). *The applied dynamics of ocean surface waves, advanced series on ocean engineering* (Vol. 1). Singapore: World Scientific.
- Miyazawa, Y., Zhang, R., Guo, X., Tamura, H., Ambe, D., Lee, J., et al. (2009). Water mass variability in the western North Pacific detected in 15-year eddy resolving ocean reanalysis. *Journal of Oceanography*, 65(6), 737–756. <https://doi.org/10.1007/s10872-009-0063-3>
- Nagai, T., Tandon, A., Kunze, E., & Mahadevan, A. (2015). Spontaneous generation of near-inertial waves by the Kuroshio front. *Journal of Physical Oceanography*, 45(9), 2381–2406. <https://doi.org/10.1175/JPO-D-14-0086.1>
- Shchepetkin, A. F., & McWilliams, J. C. (2005). The Regional Oceanic Modeling System (ROMS): A split-explicit, free-surface, topography-following-coordinate oceanic model. *Ocean Modelling*, 9(4), 347–404. <https://doi.org/10.1016/j.ocemod.2004.08.002>
- Uchiyama, Y., Kanki, R., Takano, A., Yamazaki, H., & Miyazawa, Y. (2017). Mesoscale reproducibility in Regional Ocean Modelling with a three-dimensional stratification estimate based on Aviso-Argo data. *Atmosphere-Ocean*, 1–18. <https://doi.org/10.1080/07055900.2017.1399858>

- Uchiyama, Y., Suzue, Y., & Yamazaki, H. (2017). Eddy-driven nutrient transport and associated upper-ocean primary production along the Kuroshio. *Journal of Geophysical Research: Oceans*, *122*, 5046–5062. <https://doi.org/10.1002/2017JC012847>
- Varlamov, S. M., Guo, X., Miyama, T., Ichikawa, K., Waseda, T., & Miyazawa, Y. (2015). M2 baroclinic tide variability modulated by the ocean circulation south of Japan. *Journal of Geophysical Research: Oceans*, *120*, 3681–3710. <https://doi.org/10.1002/2015JC010739>
- Venayagamoorthy, S. K., & Fringer, O. B. (2006). Numerical simulations of the interaction of internal waves with a shelf break. *Physics of Fluids*, *18*(7), 076603. <https://doi.org/10.1063/1.2221863>
- Woodruff, S. D., Slutz, R. J., Jenne, R. L., & Steurer, P. M. (1987). A comprehensive ocean-atmosphere data set. *Bulletin of the American Meteorological Society*, *68*(10), 1239–1250. [https://doi.org/10.1175/1520-0477\(1987\)068%3C1239:ACOADS%3E2.0.CO;2](https://doi.org/10.1175/1520-0477(1987)068%3C1239:ACOADS%3E2.0.CO;2)